Scientific paper

Modulation of Cerium Carbonate Crystal Growth by Polyvinylpyrrolidone using Density Functional Theory

Deyun Sun,^{1,2,3} Yanhong Hu,^{1,2,3,*} Mao Tang,^{1,2,3} Ze Hu,^{1,2,3} Peng Liu ^{1,2,3} Zhaogang Liu^{1,2,3} and Jinxiu Wu^{1,2,3}

 $^{
m 1}$ College of Materials and Metallurgy, Inner Mongolia University of Science and Technology, Baotou 014010, China;

² Key Laboratory of Rare Earth Hydrometallurgy and Light Rare Earth Application in Inner Mongolia Autonomous Region, Baotou 014010, China;

³ Key Laboratory of Green Extraction and Efficient Utilization of Light Rare Earth Resources, Ministry of Education, Baotou 014010, China

* Corresponding author: E-mail: Bthyh@163.com

Received: 08-12-2021

Abstract

Cerium carbonate crystal morphology is predicted using density functional theory (DFT) simulations in this paper. In the nucleation phase, the ketone group in polyvinylpyrrolidone (PVP) will preferentially bind to Ce3+ to form complexes and provide heterogeneous nucleation sites for the system, prompting the nucleation of cerium carbonate crystals. In the growth stage, due to the adsorption of PVP, the probability of (120) crystal plane appearing in the equilibrium state is the greatest, resulting in the formation of hexagonal flake cerium carbonate crystals with (120) crystal plane as the oblique edge. Experimentally, hexagonal sheet cerium carbonate crystals were successfully prepared using PVP as a template agent. Therefore, DFT can be used to predict the morphology of cerium carbonate crystals, which not only elucidates the growth mechanism of cerium carbonate crystals, but also greatly reduces the experimental cost.

Keywords: Cerium carbonate hydrate; Polyvinylpyrrolidone (PVP); Self-assembly template method; Density functional theory; Morphology control

1. Introduction

Rare earth ore resources in Bayan Obo, Baotou rank first in the world, with light rare earths accounting for more than 98%, while 50% of them are cerium resources. Due to its special electronic structure, cerium oxide has superior oxygen storage and redox ability. It is widely used in many fields such as electronic ceramics, polishing powder, catalyst, sensors, fuel cells, UV absorption, etc.¹⁻¹¹ It has become an indispensable material for high-tech industries and cutting-edge innovations. The cerium oxide with different morphologies has obvious functional differences, which will have a huge impact on the performance of products. Therefore, the development of industrial preparation technology of rare earth compounds with special morphology is very important. So far, cerium oxide with special morphology has been prepared by physical, chemical and many other ways at home and abroad. 12-14 Using polymers as self-assembly templates to regulate material properties provides a new idea for the artificial synthesis of crystal materials and bio-intelligent materials with special functions. 15-18

The self-assembly-template method is favored by more and more experts and scholars because of its simplicity, low cost and strong controllability. Sodium polystyrene sulfonate (PSS), nonylphenol polyoxyethylene ether (NPEO), polyallylammonium chloride (PAH), polyvinylpyrrolidone (PVP) and ethylenediaminetetraacetic acid disodium (EDTA-2Na) were used as templates in our research group. Spherical cerium oxide for catalytic materials, shuttle-shaped cerium oxide for improving glass properties, hexagonal flake cerium oxide for solid oxide fuel cells, and flower-like cerium oxide for UV absorption were prepared by self-assembly template method.^{19–22} Lin Wang et al. synthesized polyaniline (PANI) with nanoscale spherical or string-like morphology using PS-b-P2VP as a templating agent for modulation by template-self-assembly method, and the average diameter of each sample was found to be less than 200 nm and showed a tendency to decrease with increasing pH.²³ Using chitosan as a new carbon and nitrogen source precursor and triblock amphiphilic copolymer (F127) as a soft template, nitrogen-doped mesoporous carbon nanoparticles (NMCs) with pore size distribution between 3.05 and 6.09 nm were successfully prepared by Xianshu Wang et al. The analysis revealed that the nitrogen-doped mesoporous carbon materials have well-developed pores, and the nanoparticles have a spherical shape with an average diameter of about 300–400 nm and a worm-like mesoporous structure.²⁴

With the rapid progress of science and technology and the development of interdisciplinary, the method of computer theoretical calculation to synthesize new materials has attracted more and more attention of scientists. Ab initio quantum chemistry method can be used to study the nucleation mechanism and growth mode of materials from the atomic or molecular scale, and disclose the mechanism that cannot be explained in experiments. The morphology control mechanism of cerium carbonate crystals, the precursor of cerium oxide, was studied in our previous research, by molecular dynamics method, and the interaction between the template agent and the crystal surface was simulated. The relationship between the template agent and the crystalline surface of cerium carbonate crystals was revealed from the energy perspective, and the growth mechanism of cerium carbonate crystals was further disclosed.^{25–26} Ning Liu et al. successfully predicted the crystal habit of FOX-7 to be spindle-shaped under vacuum conditions with the help of molecular dynamics method. The crystalline habit of FOX-7 in H₂O/DMF solution conditions varied significantly with temperature conditions, and the crystalline habit in different ratios of solvents was blocky when the temperature was 298 K.27 Balbuena Cristian et al. studied the synthesis of silver nanoparticles with polyvinylpyrrolidone as capping agent, the nucleation of atomic clusters and the subsequent growth of nanoparticles by molecular dynamics, finding that the formation of crystals follows Ostwald ' s law of phase transition. As the process progresses, a series of ordered structures appear inside the particle: icosahedral, body-centered cubic and face-centered cubic, and finally a block-silver equilibrium configuration.²⁸

This paper uses a combination method of computational simulation and experimental research. The interaction mechanism of PVP with Ce3+ and H2O in aqueous solution before precipitation and the adsorption of PVP on the main crystal plane after precipitation were calculated and simulated. The process of morphological change of cerium carbonate crystals under the regulation of PVP is explained from the atomic point of view by analyzing the electronic structure and energy change in different cases.²⁹⁻³³ And the morphology of cerium carbonate crystals was predicted. Then, the cerium carbonate crystals were successfully prepared by the self-assembly-template method using CeCl₃ as raw material, NH₄HCO₃ as precipitant and PVP as template agent. The phase structure, morphology and dimensions of cerium carbonate crystals were characterized by Scanning electron microscope (SEM), Transmission electron microscope (TEM) and Diffraction of X-rays (XRD). The experimental results are compared and analyzed with the simulated prediction results to verify the correctness of the prediction results.

2. Material and Methods

2. 1. Experimental Materials

The cerium chloride (CeCl₃) used in this experiment was prepared by dissolving and de-hybridizing industrial cerium carbonate provided by Baogang Rare Earth High-Tech Company, Inner Mongolia, China, and hydrochloric acid (analytically pure) provided by Tianjin Damao Chemical Reagent Factory, Tianjin, China. NH₄HCO₃ and anhydrous ethanol were produced by Tianjin Beilian Fine Chemicals Development Co. Ltd., Tianjin, China, and polyvinylpyrrolidone was produced by Shanghai Maclean Biochemical Technology Co. The selected chemicals were analytically pure, which could be used without further purification. The water used in all experiments was deionized water.

2. 2. Preparation Method of Ce₂(CO₃)₃ Crystals

At room temperature, deionized water was added to a certain concentration of $CeCl_3$ solution to dilute to 0.05 mol/L, and then PVP was added to prepare the mixed solution of PVP and $CeCl_3$. After stirring at a constant speed for 15 min, 0.05 mol/L NH_4HCO_3 solution was dropped into the mixed solution of $CeCl_3$ and PVP at a certain speed by a peristaltic pump for 1 h. After dripping, the solution was stirred with a stirring paddle at constant speed for 15 minutes before aging. The precipitate obtained by aging at room temperature was filtered, washed and dried to obtain $Ce_2(CO_3)_3$ crystals. The prepared $Ce_2(CO_3)_3$ crystals were characterized by SEM, TEM and XRD.

2. 3. Characterization

XRD was performed using Bruker D8 Advance X-ray diffractometer with CuKa radiation(graphite monochromator). The crystal structure was determined using CuKa radiation(40kV, 40mA), 4° step and the geometric scanning Bragg–Brentano(θ - θ) and the angle range from 5–60°(2 θ)were performed. SEM images were taken with Quanta 400 produced by Holland JEI Company, fitted with a field emission source, and working at 15 kV. All samples were mounted on copper stubs and sputter-coated with gold prior to examination. TEM images were taken with a JEM-2100 transmission electron microscope produced by JEI Company, Netherlands, with electron diffraction selected to characterize the samples, observe the morphology and analyze the crystal structure.

2. 4. Computing Method

In this paper, the Vienna Ab Initio simulation software package^{34–37} was adopted to perform DFT calculation using GGA (Generalized Gradient Approximation) method.^{38–41} The nucleation and growth of cerium carbonate crystals before and after precipitation were studied using

the LOBSTER software package involving chemical bonding analysis. 42-43 Since Ce is in the +3 valence ionic state in cerium carbonate crystals, making only one electron in the 4f orbital. And the 4f orbitals are usually significantly lower in energy than the 5d orbitals and are accompanied by an extremely contracted radial distribution of the orbitals, exhibiting a hemi-nucleation-like property and therefore not involved in bonding.44 For the sake of brevity, the density of states (DOS) of the PBEsol+U pseudopotential considering the f-orbital electrons, DOS that treats the f-orbiting electrons as a simplified pseudopotential of the inner layer electrons, and fractional density of states (PDOS) of each element were calculated using the PBEsol function, as shown in Figure 1. Without considering the peak intensity, it is found that in the electronic structures calculated by these two methods, there is not much deviation in the positions of the peaks produced by the total and partial density of states of C, H and O, except Ce. The PBEsol+U pseudopotential is compared with the simplified pseudopotential and it is found that the spin-up α and spin-down β orbitals are not equal in energy in the 6s and 5p orbitals of Ce. The spin-up α orbitals near the Fermi energy level have DOS for f and d orbitals but not on the β orbitals and exhibit 100% spin polarization for the f orbitals. This is because Ce is not pure +3 valence, and the electrons in its 4f orbitals are partially out of domain, so there is a mixed 4f and 5d feature on the PDOS, and the f orbitals have a corresponding effect on the 6s and 5p orbitals making their α and β orbitals unequal in energy. In this way, although the mixed f-d orbitals are near the Fermi energy level, they do not interact with other elements in the cell because the f orbitals are occupied by only one electron and have low energy. Therefore, the density of states with little difference is reflected in the total DOS diagram. In view of the above situation, considering the calculation efficiency, the f-orbit electrons of Ce are selected as the simplified pseudopotential of the inner electrons in the calculation method, while PBEsol functional is selected as the functional file.44-45 Other relevant calculation parameters are as follows: the plane wave truncation energy ENCUT is 350 eV, and the point K in Brillouin zone is divided by Gamma point with grid size of $4 \times 3 \times 2$. The pseudopotential file Ce selects the simplified pseudopotential of + 3 valence, and the pseudopotential of other elements such as H, O, Cl, N, C, selects the PAW pseudopotential of +1, -2, -1, +5, + 4 valence. Until the energy difference between the two iteration steps is stabilized below 10-7 eV and the force is stabilized less than -0.05 eV/Å. Considering the spin polarization of the whole system, the Ce outer electron in the simplified pseudopotential is 6s²5p⁶, and there is no solitary electron. Therefore, the system can be represented by a single molecular orbital Ψi, which can be regarded as a closed-shell system. The whole calculation process is optimized with interatomic static force at 0 K. The optimized structure is a relatively stable ground state structure with high similarity to the experimental value.

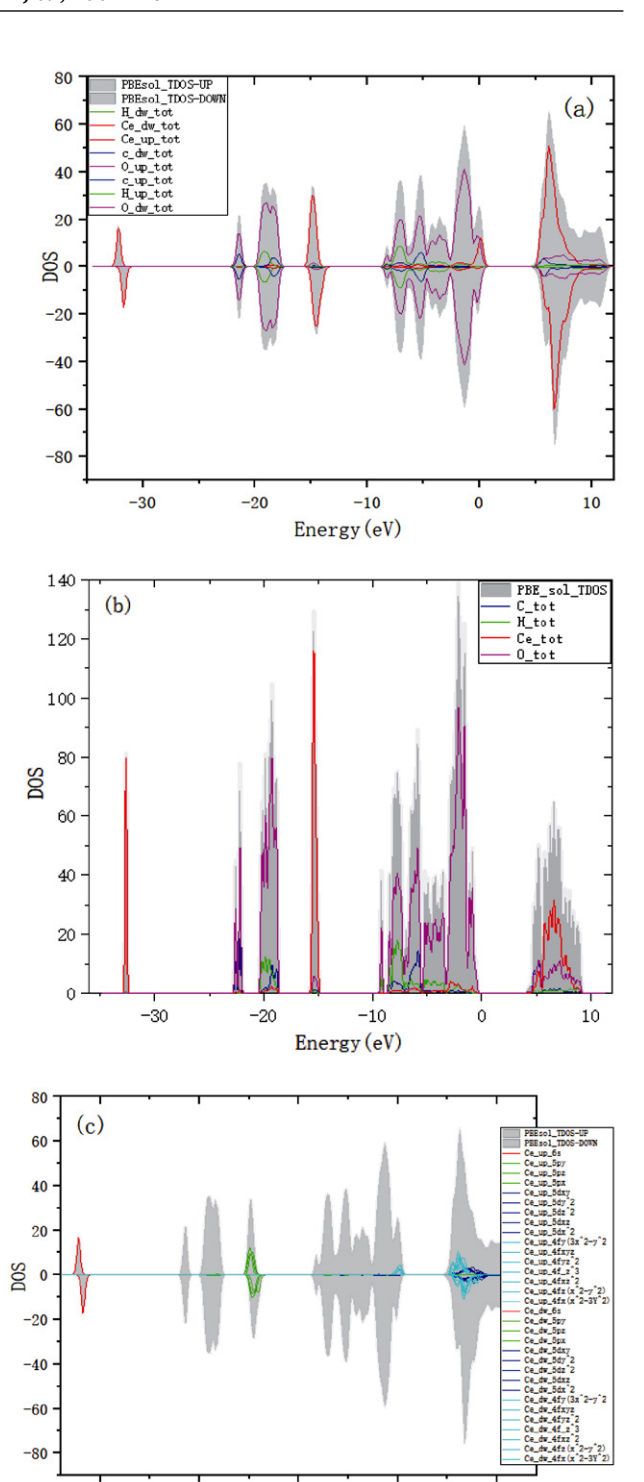


Figure 1. DOS and PDOS plots calculated by PBEsol functional (a) DOS and PDOS plots calculated by PBEsol+U pseudopotential (b) DOS and PDOS plots calculated by PBEsol simplified pseudopotential (c) PDOS plots calculated by PBEsol+U for Ce

-10

Energy (eV)

0

10

For the analysis of chemical bonds, we used the LOBSTER package to calculate the COHP (Crystal Orbital Hamiltonian) as well as the ICOHP (Integral of COHP)

-30

-20

method. COHP can obtain bonding information from the calculation results of energy band structure; the bonding, non-bonding and anti-bonding interactions between paired atoms in the material can be determined. COHP, which is the Hamiltonian matrix multiplied by the corresponding density of states matrix, is calculated as shown in equation (1),

$$\begin{split} \sum_{j} f_{j} \epsilon_{j} \delta \left(\epsilon_{j} - \epsilon \right) &= \sum_{j} f_{j} \sum_{RL} \sum_{R'L'} u_{RL,j}^{*} H_{RL,R'L'} u_{R'L',j'} \delta \left(\epsilon_{j} - \epsilon \right) \\ &= \sum_{RL} \sum_{R'L'} H_{RL,R'L'} \sum_{j} f_{j} u_{RL,j}^{*} u_{R'L',j'} \delta \left(\epsilon_{j} - \epsilon \right) \\ &= \sum_{RL} \sum_{R'L'} H_{RL,R'L'} N_{RL,R'L'} \left(\epsilon \right) \\ &= \sum_{RL} \sum_{R'L'} COHP_{RL,R'L'} \left(\epsilon \right) \end{split}$$

$$(1)$$

where f_i represents the occupation number, ε_i represents the energy band energy, R represents the atom, L represents the atomic orbital, j represents the energy band (molecular orbital), H_{RLR'L'} represents the Hamiltonian matrix element, and $N_{RL,R'L'}(\varepsilon)$ represents the DOS (density of states) matrix. Bonding contribution reduces the energy of the system, and COHP is negative; the inverse bond contribution increases the system energy, and COHP is positive; the non-key contribution is represented by the zero value of COHP. In practical applications, positive, negative and zero values of-COHP are commonly used to represent bond, anti-bond and non-bond interactions. The integral over the entire occupied orbital COHP is usually denoted as ICOHP, which allows a quantitative analysis of the bonding strength between pairs of atoms. It is defined by equation (2):

ICOHP =
$$E_{band} = \int_{-\infty}^{\varepsilon_F} \sum_{RL} \sum_{R'L'} COHP_{RL,R'L'}(\varepsilon) d\varepsilon$$
 (2)

Analysis of the absolute value of ICOHP alone has no meaning, only comparative analysis of its relative value can reflect the significance of ICOHP. In comparison, the smaller the value of ICOHP, the stronger the stability of bonding and vice versa. 43,46–47

2. 5. Modeling

During the static calculation, the system before precipitation was an aqueous solution system of CeCl₃ and polymer PVP. Scaling to a scale based on actual experimental density with "Calculation" in "Material Studio" software,⁴⁸ the slab model of the aqueous solution system mixed with CeCl₃ and polymer PVP was constructed; according to the density of 1 g/cm³, 2 Ce, 6 Cl, 20 H₂O, and 3 PVP molecular monomers were added to make them randomly distributed in the slab model. Following the above convergence criteria, we optimized the whole slab model, calculated its COHP, ICOHP, and studied the interaction

mechanism of polymer PVP monomer with other elements in the system. The mechanism of PVP modulation of cerium carbonate crystals after the addition of precipitant was simulated, and the cerium carbonate crystal structure was derived from the ICSD (Inorganic Crystal Database) crystal library as shown in Figure 2. Three crystal planes (010), (001) and (120), which are easy to be exposed were selected. According to the atomic ratios of the cerium carbonate crystal, the crystal plane layers with thickness of 9.3546 Å, 9.037 Å and 7.989 Å were cut respectively. These atomic layers were put at the bottom to construct a slab configuration with a top vacuum layer thickness of 13 Å. According to different thickness, the atoms at the bottom of each crystal plane are fixed at a ratio of 60%, and the rest are released. (001) crystal plane is fixed from the bottom with 0-9.4 Å thickness atoms; (010) crystal plane is fixed from the bottom with 0-5.4 Å thickness atoms; (120) crystal plane is fixed from the bottom with 0-4.8 Å thickness atoms. The entire slab configuration is optimized according to the above convergence criteria and meets the relevant convergence requirements.

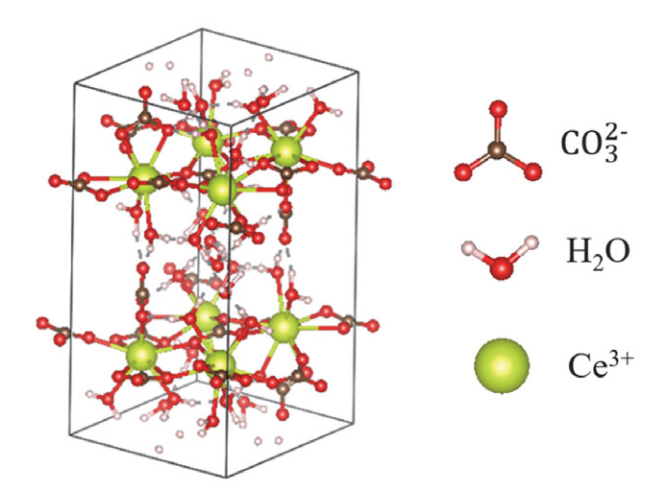


Figure 2. $Ce_2(CO_3)_3$ crystal structure diagram, in which the green ball represents the Ce element, and each Ce element is surrounded by 4 carbonate ions and 4 water molecules

In the AIMD (Ab Initio Molecular Dynamics) simulation, $^{49-51}$ using "Calculation" function in "Material Studio" software, scaling based on actual experimental density in a certain proportion, the slab model of mixed aqueous solution system of Ce^{3+} , Ce_3^{2-} nd polymer PVP monomer was constructed. According to the density of 1 g/cm³, 8 Ce^{3+} , 12 Ce_3^{2-} , 20 H_2O and 2 PVP polymer monomers were added to make them randomly distributed in the slab model. The nucleation and growth of $Ce_2(CO_3)_3$ crystals in solution were analyzed by molecular dynamics simulations, and the set of uniformly distributed Ce^{3+} Ce_3^{2-} and H_2O in the slab model was used as the initial configuration. The NVT ensemble at 300 K is selected, and these values

represent the synthesis conditions in the experiment. The total simulation time for the equilibrium motion was 1500 ps with a time step of 1 fs, during which data were collected every 500 ps for subsequent analysis.

In the optimization of PVP molecules, considering that the use of DFT calculations for macromolecular polymers will occupy too many resources, while the electronic structure analysis of the crystal surface only needs to consider the interaction between a small part of the crystal and the polymer monomer atoms, and the PVP polymer monomer has similar properties to the PVP polymer, only the PVP polymer monomer (Figure 3) was taken for structural optimization, and then its adsorption relationship with the crystal surface and subsequent electronic structure analysis were investigated.

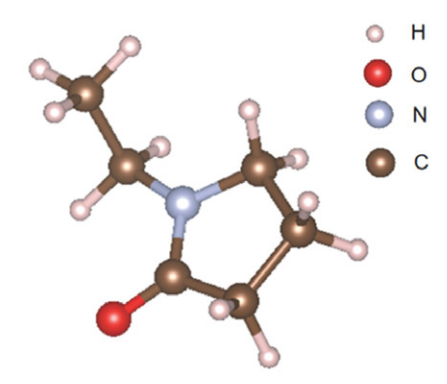


Figure 3. Schematic diagram of PVP monomer molecule

3. Results and Discussion

3. 1. Mechanism Study

3. 1. 1. The Interaction Mechanism of PVP in the System Before Precipitation

In the constructed slab model, the results before and after optimization are shown in Figure 4. The two Ce^{3+} in

the constructed slab model are #7_Ce and #8_Ce, respectively, and it is found that the PVP, H₂O and Cl⁻ in the system are gradually aggregated around Ce³⁺, in which C=O in PVP, O in H₂O, and Cl⁻ will interact around the center Ce³⁺ with a tendency to form bonds, while H atoms in H₂O will form hydrogen bonds with C=O in PVP. As the atoms move to the position where the force is the least, the atoms in the entire system will aggregate toward the Ce³⁺ position to form the corresponding complex. The ICOHP and bond lengths between the major bond-forming atoms in the system are shown in Table 1. The analysis revealed that although the bond length of the chemical bond formed between PVP-Ce³⁺was the longest, its ICOHP value was the smallest. It is because of the large atomic radius and atomic mass of Ce³⁺, and its unique electronic structure as well as chemical properties. Thus, although the bond length between PVP-Ce³⁺ is the longest, the stability is stronger than that between PVP-H₂O and H₂O-H₂O to form chemical bonds. This shows that the bonding effect between Ce3+ and PVP is the greatest, so when no precipitation agent is added, the PVP molecules in the system will preferentially complex with Ce^{3+} to form a more stable complex.

Table 1. The bond length and ICOHP value between each atom after the optimization before precipitation is completed

| atomNU | atomNU | bond length (Å) | -ICOHP(eV) |
|----------|------------------|-----------------|------------|
| O in PVP | Ce ³⁺ | 2.38 | -3.57 |
| O in PVP | H_2O | 1.65 | -1.17 |
| H_2O | H_2O | 1.86 | -0.90 |

3. 1. 2. Analysis of Crystal Planes Easily Exposed Without Polymer PVP

According to the research results of Li Erxiao and others,²⁶ crystal planes easy to display in PVP adsorption cerium carbonate crystal were selected, and the (001), (010), (120) crystal planes before and after the

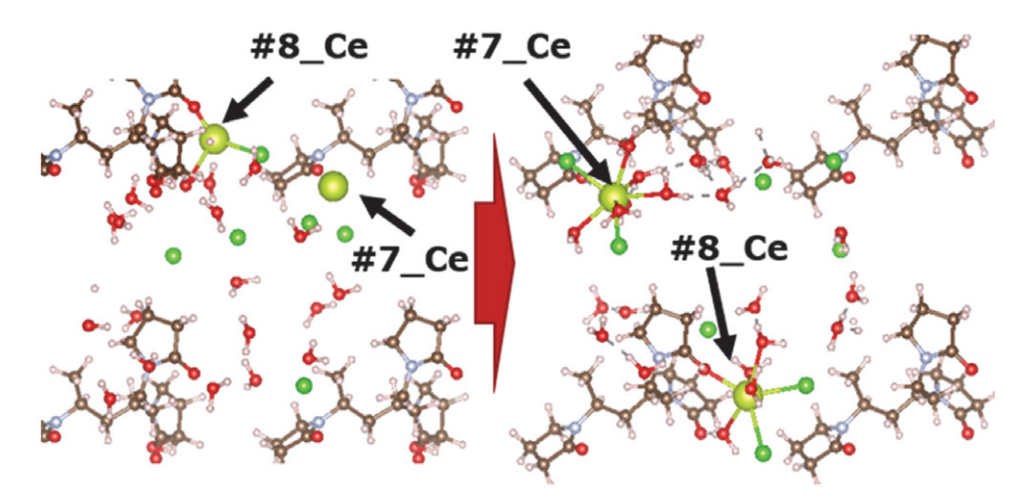


Figure 4. Optimization diagram of each atom in the system before precipitation

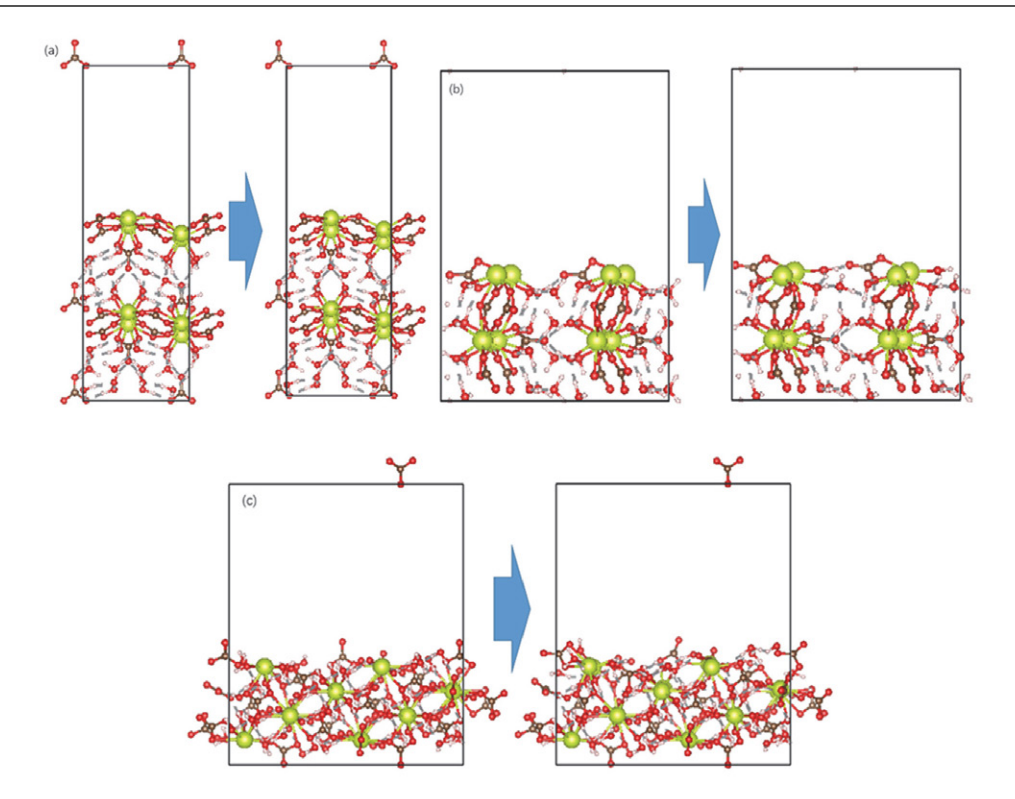


Figure 5. (a) cerium carbonate crystal (001) crystal plane before and after optimization, (b) cerium carbonate crystal (010) crystal plane before and after optimization, (c) cerium carbonate crystal (120) crystal plane before and after optimization

optimization of each crystal plane cut out are shown in Figure 5. It is found that after the optimization of these three crystal planes, the reconstruction of the crystal planes has occurred, and the bonding distance between the surface layer atoms and the bottom layer atoms has slightly increased. This is because the top of the constructed surface is in a vacuum layer. The surface atoms are only subject to the interaction between themselves and the bottom atoms, resulting in different forces from the internal atoms.

The formula for calculating the surface energy of crystal plane is shown in Formula 1,⁵² where σ is the surface energy of the crystal; E^{rel} is the relaxation energy, indicates the energy released when the crystal plane is optimized to a stable state; E_{surf} is the energy of the slab configuration after optimization; Natoms is the number of atoms in the slab configuration; E_{bulk} is the energy of a single atom in the bluck structure and represents the ratio of the energy of the unit cell to the number of atoms in the unit cell after optimization. The calculated results of (001), (010) and (120) crystal planes are shown in Table 2, indicating that the surface energy of the (120) crystal plane was the lowest, 9.48 J/m², and its growth rate was the slowest; the (001) crystal plane had the highest energy, 17.1 J/m², and its growth rate was the fastest. The order of growth speed between crystal planes is (001) > (010) > (120).

$$\sigma = (1/2 (E_{surf} - N_{atoms} * E_{bulk}) + E^{rel}) / A (3)$$

Table 2. Relative crystal plane parameters of crystal planes easily exposed when PVP is not added

| planes | E ^{rel} (meV) | N _{atoms} | E _{surf} (eV) | E _{bulk} (eV) | A (Å ²) | σ (J/m ²) |
|--------|------------------------|--------------------|------------------------|------------------------|------------------------|--------------------------|
| 001 | 2.19 | 152 | -766.41 | -6.11 | 77.23 | 17.1 |
| 010 | 3.94 | 152 | -748.27 | -6.11 | 133.29 | 11.1 |
| 120 | 1.36 | 304 | -1514.18 | -6.11 | 301.35 | 9.48 |

3. 1. 3. Analysis of Crystal Planes Easily Exposed after Adding Polymer PVP

Figure 6 shows the adsorption structure diagram of the PVP monomer on the (001), (010), (120) crystal planes of cerium carbonate crystals after calculation by DFT. The length of the Ce-O bond formed by the O contained in the ketone group in the PVP monomer and the Ce³⁺ of the (010) crystal plane is the smallest, 2.37 Å, while the Ce-O bond length formed by O and Ce³⁺ of (120) crystal plane is the longest, 2.42Å. The Ce-O bonds after adsorption is shorter than the Ce-O bonds in the cerium carbonate crystal. From the analysis of the C-O bonds length inside the PVP monomer, it is found that, except for the (001) crystal plane adsorption which causes the C-O bonds bond length to remain unchanged, the (010) and (120) crystal plane adsorption will cause the C-O bonds bond length to be elongated. From the analysis of the Ce-O-C bonds angle

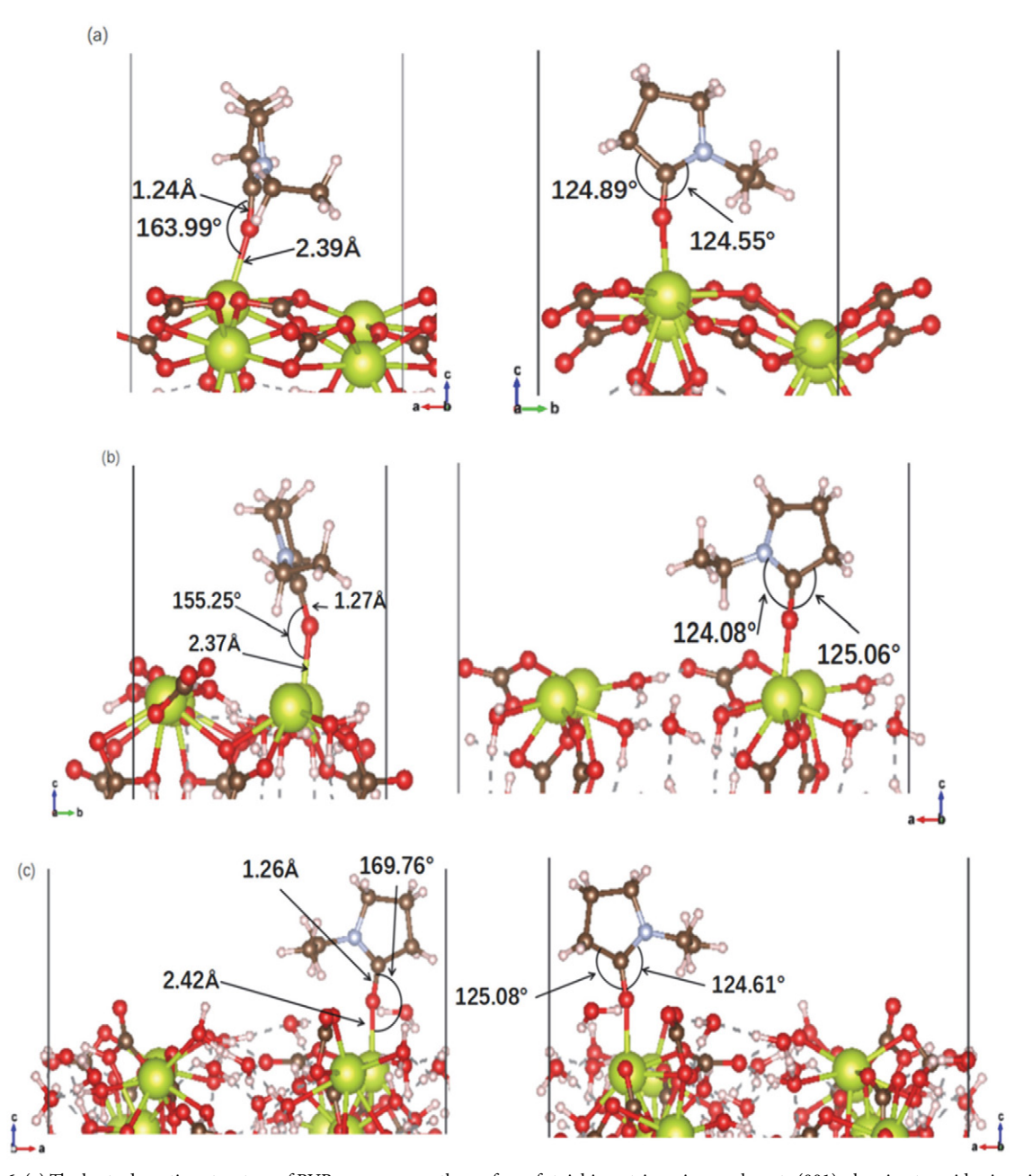


Figure 6. (a) The best adsorption structure of PVP monomer on the surface of stoichiometric cerium carbonate (001), showing two side views in the plane model, (b) the best PVP monomer on the surface of stoichiometric cerium carbonate (010) Adsorption structure, showing two side views in the plane model, (c) the best adsorption structure of PVP monomer on the surface of stoichiometric cerium carbonate (120), showing two side views in the plane model

formed by the adsorption of Ce³⁺ from the PVP monomer ketone group, it is found that the bond angle formed by the adsorption of the (010) crystal plane is the smallest, 155.25°, and the bond angle formed by the adsorption of the (120) crystal plane is the largest, 169.76°. From the analysis of the bond angles of O-C-N and O-C-C bonds formed inside PVP monomer after adsorption, it is found that the bond angles of O-C-N bonds and O-C-C bonds after adsorption are smaller than the bond angles before adsorption. It is because the Ce-O bond formed by the ketone group and Ce³⁺ in PVP monomer after adsorption

has a certain interaction with C and N attached to O inside PVP monomer, which makes the bond angle smaller in general.

The adsorption energy of the molecules adsorbed on the crystal surface calculation is shown in formula $2,^{52}$ where E_{bind} is the adsorption energy of PVP adsorbs the cerium carbonate crystal face, E_{tot} is the total energy of the system after PVP adsorbs the cerium carbonate crystal face, and E_{solv} is the single point energy of the PVP monomer. E_{surf} is the total energy of the cerium carbonate crystal face system without adsorption of

PVP monomer. The crystal planes calculated according to Formula 2 are shown in Table 3. The adsorption energy of each crystal plane is analyzed. When the adsorption energy is positive, additional absorption energy is required for the occurrence of adsorption, and when the adsorption energy is negative, the energy is released. The definition of adsorption indicates that the adsorption energy of whichever crystal plane and PVP monomer is negative. It shows that the PVP monomer needs to release energy after adsorbing (001), (010), (120) crystal planes. Comparing the size of adsorption energy, it is found that the adsorption energy of (120) crystal plane is the largest. The adsorption energy difference between (001) and (010) crystal planes is only about 2eV, indicating that PVP molecules are more likely to adsorb (120) crystal planes during the growth of cerium carbonate crystal, and inhibit the growth of crystal planes, so that they can finally be exposed.

$$E_{\text{bind}} = E_{\text{tot}} - (E_{\text{solv}} + E_{\text{surf}}) \tag{4}$$

Table 3. After adding PVP, PVP monomer and easy to show surface adsorption related energy parameter table

| planes | E _{tot} (eV) | E _{solv} (eV) | E _{surf} (eV) | E _{bind} (eV) |
|--------|-----------------------|------------------------|------------------------|------------------------|
| 001 | -1023.43 | -110.31 | -768.60 | -144.51 |
| 010 | -1008.87 | -110.31 | -752.21 | -146.34 |
| 120 | -1930.42 | -110.31 | -1527.74 | -292.37 |

3. 1. 4. Electronic Structure Analysis of the Growth Mechanism of Cerium Carbonate Crystals Regulated by PVP

In order to further study the interaction mechanism between PVP and cerium carbonate crystal surface, the COHP value of PVP monomer adsorption on different crystal faces was calculated, and its electronic structure was analyzed. When cerium ions are exposed on the crystal surface, the central cerium ion loses two water molecular ligands along the +b axis, which reduces the original 10-ligand structure (Figure 7a) to an 8-ligand structure (Figure 7b), and coordination unsaturation occurs, therefore the cerium ions have a greater tendency to be adsorbed by the polar element O in the system.

The COHP of each crystal plane adsorbed by PVP is shown in Figure 8, and the COHP value of each crystal plane adsorbed by PVP monomer is analyzed. It is found that the three crystal planes (001), (010), and (120) have basically the same bonding conditions after adsorption of the PVP monomer, only when the (100) crystal surface is adsorbed, a negative peak of -COHP value appears near the fermi level, which indicates that there is an unstable component at this position. Because the peak is small, it almost has no effect on the bonding stability. Compar-

ing the ICOHP value after PVP adsorption on each crystal plane, the ICOHP value of (120) crystal plane is the smallest, which is -3.49eV, indicating that the stability of PVP monomer and (120) crystal plane adsorption is the strongest.

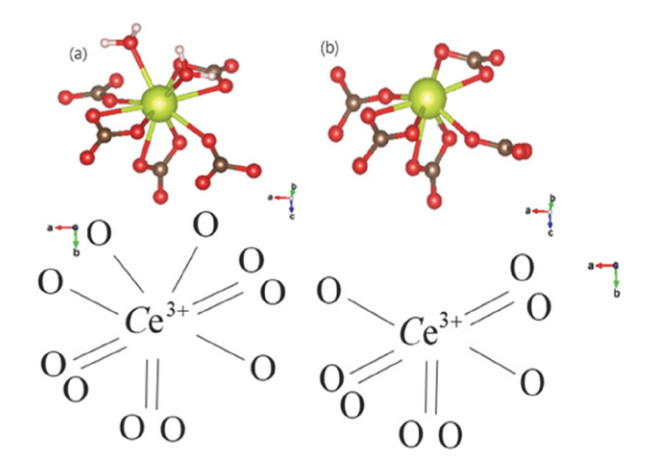


Figure 7. (a) 10 ligand structure diagram; (b) 8 ligand structure diagram

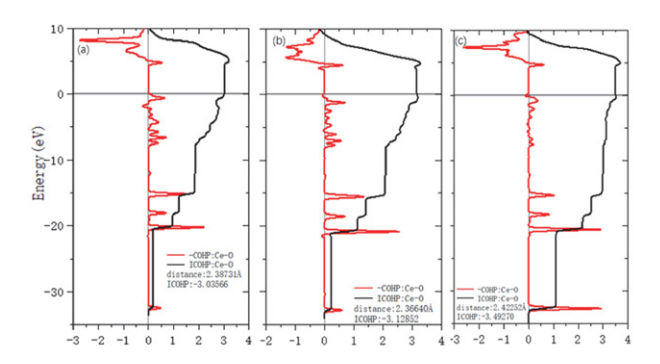


Figure 8. (a) PVP monomer adsorption (001) crystal plane COHP map, (b) PVP monomer adsorption (010) crystal plane COHP map, (c) PVP monomer adsorption (120) crystal plane COHP map

3. 1. 5. AIMD Simulation of Growth Process of Cerium Carbonate Crystals Regulated by PVP

In this section, an ab initio molecular dynamics (AIMD) method is used to simulate the process of PVP regulating the growth of cerium carbonate crystals at the atomic scale. Figure 9 shows sequential snapshots of the complex formed by Ce_3^{2-} and PVP and Ce^{3+} from the initial state to 1500ps. In the initial state, the atoms are uniformly distributed in the system. With the passage of simulation time, Ce_3^{2-} gradually shifts to the heterogeneous nucleation site formed between PVP and Ce^{3+} . When the simulation time reaches 1500ps, it can be seen that growth of cerium carbonate crystals along the PVP adsorption direction is inhibited, leading to the growth of cerium carbonate crystals in other directions.

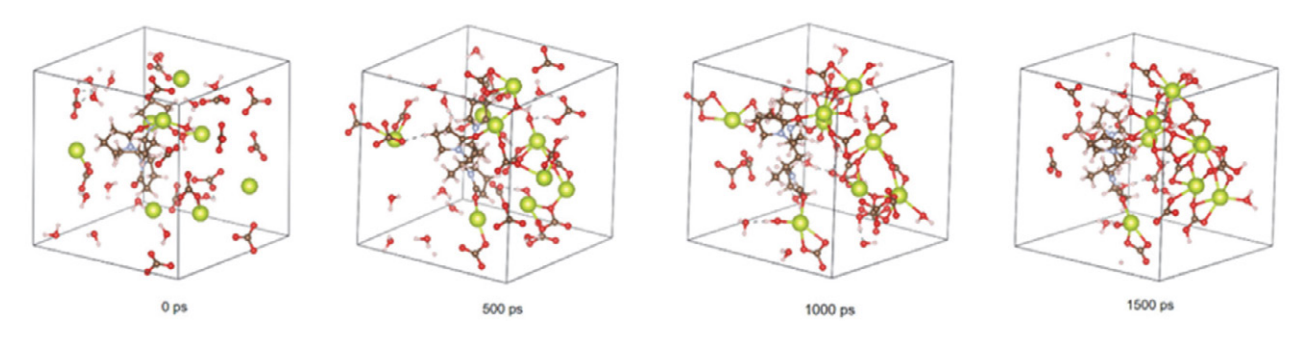


Figure 9. Snapshot of AIMD simulation of PVP-controlled cerium carbonate crystal growth process at 300K

3. 2. Simulation of PVP Controlling Cerium Carbonate Crystal Growth Process

Figure 10 is a simulation process diagram of using polymer PVP liquid phase precipitation method to control the morphology of cerium carbonate crystals, which is mainly divided into the following three stages:

1. In the first stage, $CeCl_3$, PVP and H_2O are added to the slab configuration and optimized to a stable state. The

ketone groups in the system and PVP will preferentially form complexes, providing heterogeneous nucleation sites for subsequent crystal crystallization.

2. In the second stage, with the addition of precipitant, the complex formed by PVP and Ce^{3+} is combined to produce heterogeneous nucleation. With the continuous addition of the precipitating agent, Ce_3^{2-} combines at the heterogeneous nucleation point where PVP molecules

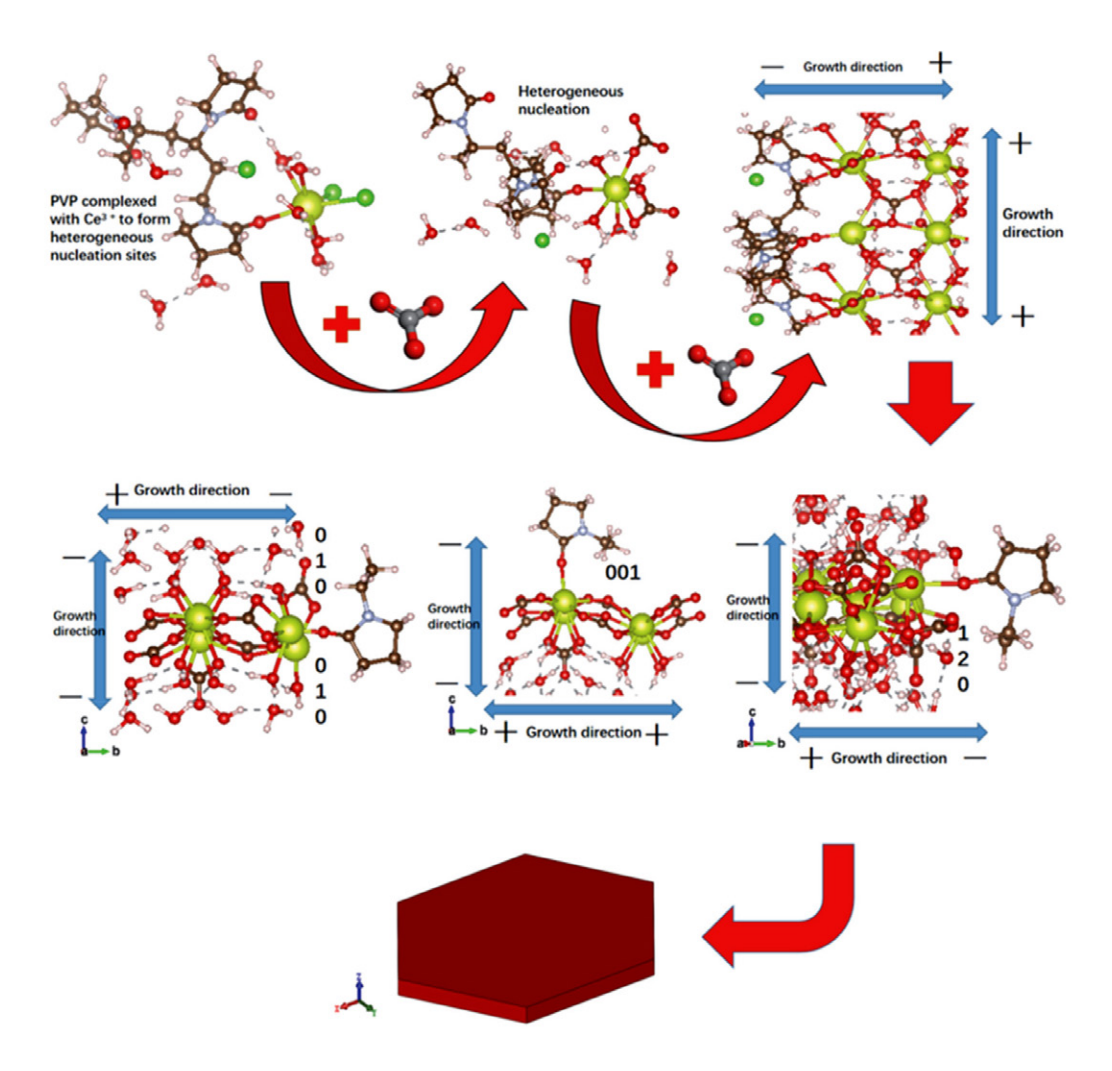


Figure 10. Process diagram of PVP regulating cerium carbonate crystal growth

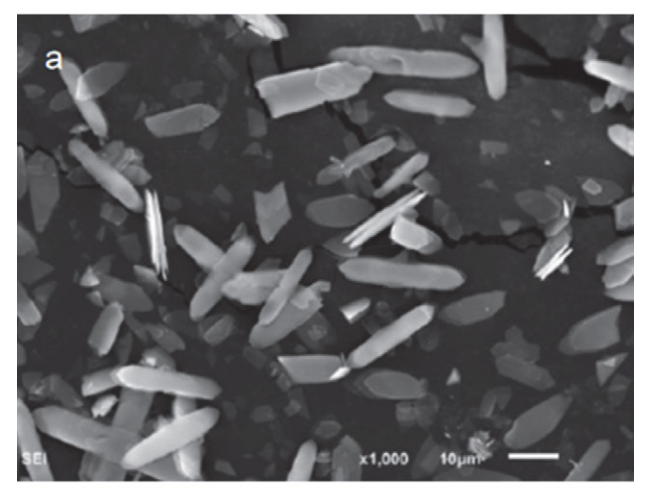
are adsorbed and gradually grows into cerium carbonate crystals. In the process of crystal growth, according to the symmetry of cerium carbonate crystal PBNB, the growth of (010) crystal plane along the C axis and + B axis is inhibited, (001) crystal plane along the C axis is inhibited, (120) crystal plane along the axis (210) and C axis is inhibited. Moreover, the (120) crystal plane has the strongest PVP adsorption ability and the slowest growth rate, making the (120) crystal plane most likely to appear in the system.

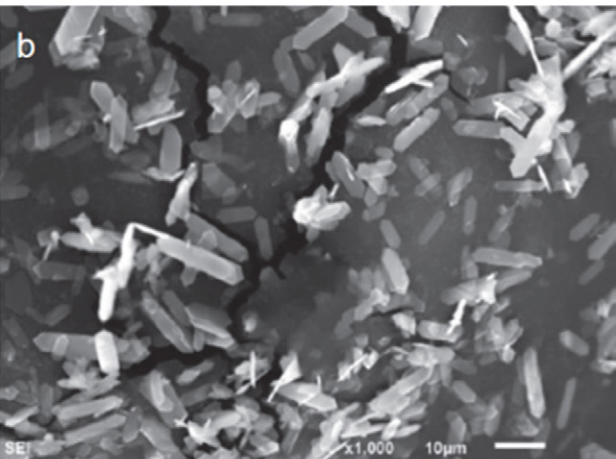
3. In the third stage, after crystal gradually fills the whole solution system, each crystal face fragment will combine with each other. According to the classical crystal growth theory,⁵³ the crystal face with a faster growth rate will disappear, while the crystal face with a slower growth rate will eventually remain. For the PVP molecules are adsorbed on the (120) crystal plane and hinder the (120) crystal plane, the growth rate of (120) crystal plane is the slowest compared with other crystal planes such as (001) and (010) crystal planes, so the (120) crystal plane has a greater probability of being retained, and each crystal face finally grows around the (120) crystal face into a hexagonal plate-shaped cerium carbonate crystal.

3. 3. Experimental Verification Analysis

3. 3. 1. SEM Analysis of Products in Different Growth Stages of Cerium Carbonate Crystals

Figure 11 shows the SEM images of the cerium carbonate crystal morphology prepared using the liquid phase precipitation method, with CeCl₃ as the Ce source, PVP as the template, NH₄HCO₃ as the precipitant, when the Ce³⁺ concentration is 0.03M, the pH value of the initial solution is 2, and the R value (The ratio of Ce₃²⁻ to Ce³⁺) is about 2:1. Figure 11 (a) is the SEM image obtained when the precipitating agent (NH₄HCO₃) is added dropwise for 10 minutes. At this time, the cerium carbonate crystals are slightly rounded at both ends, slender and fusiform, without obvious edges and corners. This is because at early reaction stage cerium carbonate crystal grows into an amorphous state, and the crystal lattice is not perfect yet. Figure 11 (b) is the SEM image obtained when the precipitating agent (NH₄H-CO₃) is dropped for 30 minutes. The cerium carbonate crystals have been transformed from the original fusiform shape to the angular, narrow and long hexagonal flake. With the extension of the precipitant dropping time, the morphology of the cerium carbonate crystals remained in the shape of hexagonal flake, and the length of each side changed significantly. The length of the sides on both sides of the tip part gradually became longer, and the length of the length direction gradually became shorter. It indicates that the growth process of cerium carbonate crystals is regulated by PVP. At the beginning of the reaction, because the reaction speed is too fast, PVP has not yet played a regulatory role. Cerium carbonate crystals rapidly nucleate and grow into a long and narrow spindle shape. As the reaction progresses, PVP is selectively adsorbed on the crystal surface of cerium car-





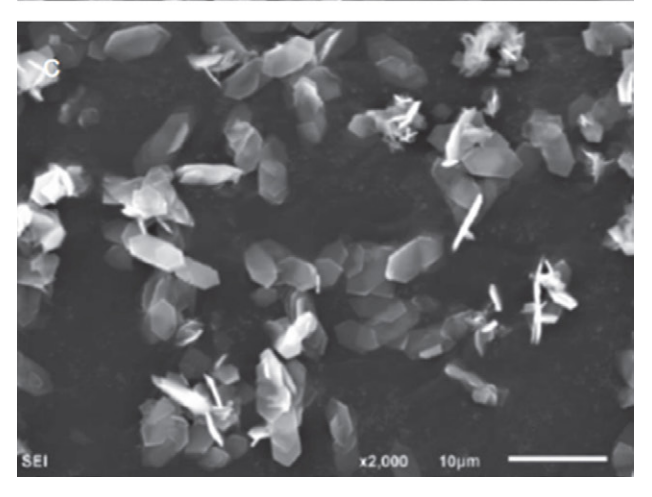


Figure 11. SEM images of different reaction stages of cerium carbonate crystals: (a) 10 min, (b) 30 min, (c) 50 min

bonate, which makes Cerium carbonate crystals eventually grow into hexagonal flake.

3. 3. 2. Analysis of Crystal Morphology

Figure 12 shows the transmission electron microscopy (TEM) of the hexagonal flake cerium carbonate crystal.

From the figure, it can be measured that the angles formed by each plane of the hexagonal flake cerium carbonate crystal are about 90° and 135°. Since the cerium carbonate crystal belongs to the orthorhombic system, formula 3 can be used to calculate the angle of each crystal plane, where $\cos \varphi$ is the cosine of the angle between the two crystal planes, $(h_1 k_1 l_1)$, $(h_2 k_2 l_2)$, is the crystal plane index of two crystal planes. The unit cell parameters obtained from PDF card (#38-0377) are: a = 9.482 Å, b = 16.938 Å, c = 8.965 Å. The cosine values of the angles between the crystal planes are listed in Table 4 (Supplementary materials).

$$cos\varphi = \frac{\frac{h_1h_2}{a^2} + \frac{k_1k_2}{b^2} + \frac{l_1l_2}{c^2}}{\sqrt{\left(\frac{h_1^2}{a^2} + \frac{k_1^2}{b^2} + \frac{l_1^2}{c^2}\right) \times \left(\frac{h_2^2}{a^2} + \frac{k_2^2}{b^2} + \frac{l_2^2}{c^2}\right)}}$$
(5)

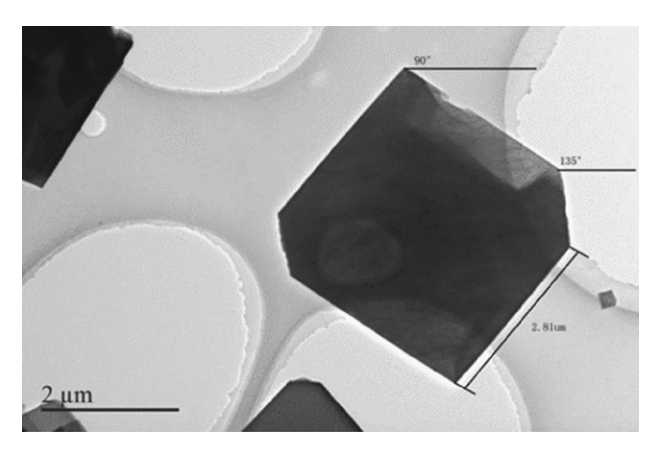


Figure 12. Transmission electron microscope image of hexagonal flake cerium carbonate crystal

The diffraction pattern of hexagonal flake cerium carbonate crystal is shown in Figure 13. According to the measurement of the ruler in the diffraction pattern from near to far, the distance R between the surrounding spots and the central spot is calculated. According to d=1/R, the crystal plane spacing d of each spot around the center diffraction spot is calculated, and the PDF card (#38-0377) of the cerium carbonate crystal is found to preliminarily

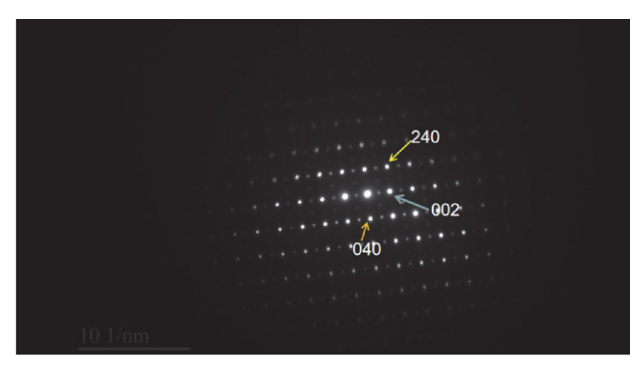


Figure 13. Diffraction pattern of hexagonal flake cerium carbonate crystal

determine the crystal plane represented by each spot. According to the angles of crystal planes measured in Figure 12, it is determined that the sides of the hexagonal flake cerium carbonate crystal are (002), (040), and (240) respectively by looking up Table 4 (Supplementary materials).

Figure 14 shows XRD images of cerium carbonate crystals regulated by PVP. The four strongest peaks are (020), (040), (060), and (200) crystal planes. These four crystal planes belong to the {100} crystal plane family. Because (240) crystal plane is inclined plane of hexagonal flake crystal, the intensity of (240) crystal plane peak is relatively weak in XRD. Therefore, the hexagonal flake cerium carbonate crystal with (240) crystal plane as inclined plane and {100} crystal plane group as top and side can be seen in the SEM.

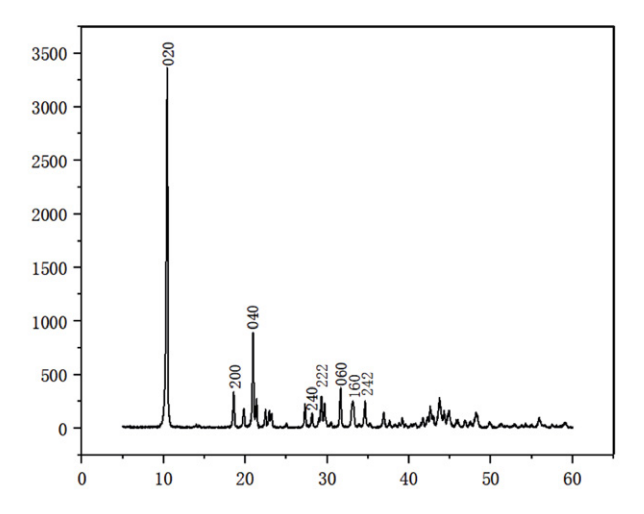


Figure 14. XRD pattern of hexagonal flake cerium carbonate crystal

4. Conclusions

The morphology of cerium carbonate crystal controlled by PVP was simulated by computer. When adding PVP without precipitating agent, the ketone group in PVP would preferentially complex with Ce³⁺. After adding precipitant, heterogeneous nucleation points of cerium carbonate crystal would be formed around the complex, and the cerium carbonate crystal would grow gradually around the nucleation points. By calculating the interaction relationship between exposed Ce³⁺ and polymer PVP on three crystal faces of cerium carbonate (120), (010) and (001), it is found that the absolute value of adsorption energy of (120) crystal surface is the largest, and the gap of adsorption energy of (010) and (001) is only about 2eV, which indicates that due to the adsorption of PVP in the growth process of cerium carbonate crystal, the growth resistance of the (120) plane is much greater than that of the (010) and (001) plane. In the equilibrium state, the probability of forming (120) crystal plane is the greatest, thus the hexagonal plate-like cerium carbonate crystal structure

that grows around the (120) crystal plane will eventually appear. The experimentally prepared cerium carbonate crystals were analyzed by SEM, TEM, and XRD. The morphology of the prepared cerium carbonate crystals is a hexagonal sheet-like cerium carbonate crystal with (240) crystallographic planes as bevels and {100} crystallographic families as top and sides. It is found that the morphology of cerium carbonate crystal prepared in the experiment was similar to that of cerium carbonate crystal simulated by computer. Therefore, density functional theory can be used to predict the morphology of cerium carbonate crystals, which not only elucidates the growth mechanism of cerium carbonate crystals, but also greatly reduces the experimental cost.

Acknowledgments

The financial support from National Science Foundation of China (21666029); Ministry of education innovation team project (IRT1065); Inner Mongolia Natural Science Foundation (2016MS0223); grassland talents individual training project; Inner Mongolia Autonomous Region Science and Technology Major Project (2019ZD023) is gratefully acknowledged.

5. References

- T Z Gao, X L Yu, Y X Zhang, S Q Zhang, F Zhou, L Nie. Preparation and UV-Shielding Properties of Ceria with Different Morphologies. Wet Metallurgy, 2018,37(06):497–500. DOI:10.13355/j.cnki.sfyj.2018.06.014.
- Z M Wang, X L Zhu, Y M Li, Z Y Shen, J L Zuo. Controllable preparation of flake and spherical CeO₂ nanoparticles and their photocatalytic properties. Journal of Artificial Crystals, 2017,46(08):1559–1563+1586.

DOI:10.1088/1475-7516/2017/08/022

- YN Feng, JZ Gan, XH Chen, J Zhang, HJ Duan, ZX Cui, YQ Xue. Study of morphology and particle size on the photocatalytic degradation of salt-based magenta by cerium dioxide nanoparticles. Applied Chemical Industry, 2019,48(01):14–17. DOI:10.16581/j.cnki.issn1671-3206.2019.01.002
- 4. SD Huang, GS Yang, CR Zhang, W Zhou, Y Zhao, LT Liu, L Cheng, Y Du, Z Wang, YJ Men. Rare earth polishing powder and its preparation method. CN112080207A. 2020–12–15.
- EW Liang, B Wang, SS Zhang, Z Feng, MY Liu. Research on the preparation process and color development mechanism of rare earth polishing powder. Rare Earths, 2020,41(04):102– 110. DOI: 10.16533/J.CNKI.15-1099/TF.202004013
- GF Gu, XT Cao, MH Liu, XL Wang, HQ Wan, SR Zheng, ZY Xu. Study on the catalytic performance of Pd-M/CeO₂ catalyst for toluene. Environmental Science and Technology, 2020,43(11):110–115.

DOI:10.19672/j.cnki.1003-6504.2020.11

HH Ding. Liquid-phase preparation of CeO₂ and its composites and their catalytic applications. Shanghai University of

- Engineering and Technology, Shanghai, 2018.
- 8. HJ Li. Hydrothermal synthesis of micro/nano cerium dioxide with different morphology and its properties. Anhui University, Hefei, 2018.
- 9. D Zhao. *Design and catalytic performance study of ceri-um-based nanomaterials*. Liaoning University of Petroleum and Chemical Technology, Fushun, **2020**.
- 10. J Feng, HL Chen, XM Zhang. Controlled morphology synthesis of cerium dioxide nanoparticles and their catalytic properties. Chemical Environmental Protection, 2018,38(05):559–564.
- 11. Q Hu. Preparation and performance study of one-dimensional semiconductor oxide-based methanol gas sensors. Lanzhou University, Lanzhou, **2020**.
- T Li. Study on the reaction crystallization process and crystal morphology control of cerium carbonate. South China University of Technology, Guangzhou, 2020.
- W Xu, ZH Lin, PF Hu, ZW Jin, Y Chen, CJ Qiu. Controlled synthesis of cerium oxide nanoparticles and their polishing properties. Shandong Chemical, 2020,49(02):30–32.
 DOI:10.19319/j.cnki.issn.1008-021x.2020.02.010
- 14. CS Li, YX Chen, WX Li, QG Ren, FQ Fan, F Ye, M Sun. Ultrasound-assisted synthesis of cerium oxide nanoparticles and their tribological properties. New Chemical Materials, 2019,47(S1):154–157.

DOI: CNKI:SUN:HGXC.0.2019-S1-034.

- MM Du. Superstructure self-assembly based on RhuA protein programmable. University of Science and Technology of China, Hefei, 2021.
- 16. Y Zhang. Self-assembly, property regulation and template effect of nanocellulose. Qilu University of Technology, Jinan, **2020**.
- 17. J L Xie. Self-assembly of colloidal particles into large-size colloidal fibers by controlled crack growth. University of Electronic Science and Technology, Chengdu, 2020.
- 18. J L Qin, QY Li, R Yang, ZY Qiao, Y Liu, DR Gao, TY Chang, XP Jia, XF Zhao, YZ Zhang, XF Cheng. Design and synthesis of amphiphilic polyurethanes and study of their assembly behavior. Shandong Chemical, 2020,49(02):1–4+9.

DOI: 10.19319/j.cnki.issn.1008-021x.2020.02.001

- X Zhang. Molecular dynamics study of NPEO-regulated cerium carbonate crystal growth. Inner Mongolia University of Science and Technology, Baotou, 2020.
- 20. L Xu, YH Hu, M Li, ZG Liu, MT Wang, XW Zhang, T Tian. Study on the morphology of cerium carbonate particles regulated by ethylenediaminetetraacetic acid disodium template. Rare Earths, 2019,40(05):84–90.

DOI: 10.16533/J.CNKI.15-1099/TF.201905011

 EX Li, YH H, M Li, ZG Liu, MT Wang, XW Zhang, WJ Zuo, X Zhang. Synthesis of Cerium Carbonate with Special Morphology Controlled by Polyvinyl Pyrrolidone. Chemical Progress, 2019,38(09):4212–4217.

DOI: 10.16085/j.issn.1000-6613.2018-2390

- 22. Y Zhang. Study on the Mechanism of PAH Regulating Rare Earth Carbonates with Special Morphologies. Inner Mongolia University of Science and Technology, Baotou, 2015.
- 23. L Wang, YH Zhang, MESLM Aziguli, HD Lan. Induced modulation of polyaniline morphology, size and electrochemical

- properties using PS-b-P2VP as a template agent. Journal of Higher School Chemistry, **2019**,40(08):1748–1756. **DOI**: CNKI:SUN:GDXH.0.2019-08-024
- 24. XS Wang, H Wu, RQ Xie, HY Pan, Q Lin. Preparation of nitrogen-doped mesoporous carbon spheres with tunable pore structure by chitosan-F127 soft template method. Journal of Artificial Crystals, 2019,48(04):737–744.
 - DOI: 10.16553/j.cnki.issn1000-985x.2019.04.029.
- 25. X Zhang, YH Hu, M Li, ZG Liu, M Tang, Z Hu. Molecular dynamics simulation of the crystal growth mechanism of cerium carbonate regulated by nonylphenol polyoxyethylene ether. Rare Earths, 2021,42(05):68–74.
- EX Li. MS simulation study on the mechanism of PVP-regulated cerium carbonate growth. Inner Mongolia University of Science and Technology, Baotou, 2019.
- 27. N Liu, C Zhou, ZK Wu, YJ Shu, BZ Wang, QL Zhao, WL Wang. Prediction of the crystalline morphology of FOX-7 in H2O/DMF solvent. Energetic materials, 2018, 26(06): 471–476.
- Balbuena Cristian, Gianetti Melisa Mariel, Soulé Ezequiel Rodolfo. Molecular dynamics simulations of the formation of Ag nanoparticles assisted by PVP. Physical chemistry chemical physics: PCCP 23.11(2021). DOI:10.1039/D1CP00211B
- 29. YF Yu. Theoretical study on the kinetics of graphene epitaxial growth on Ni(111) surface. Shandong University, Jinan, 2020.
- 30. SL Yuan, H Zhang, DJ Zhang. Molecular simulation: theory and experiment. Beijing: Chemical Industry Press, 2016: 162.
- 31. JT Cai, DX Li, BL Liu, BS Guo, DQ Wei, H Wang. *Molecular dynamics simulation of controlled crystallization of urea (520) crystal plane.* CIESC Journal, **2019**, 70(1): 128–135.
- 32. XQ Tang, XM Liu, Y Chen, JH Chen. *Density functional theory study on lead activation and xanthate adsorption on sphalerite surface*. Nonferrous Metal Engineering, **2021**,11(03):90–95. **DOI**: CNKI:SUN:YOUS.0.2021-03-014.
- 33. Q Ren, Y Liu, T Gao, ZX Zhou, CS Zhao, HF Chai. Study on the crystal structure and density functional theory of diethyl 2,2-bis (4-chloro-2-fluorobenzyl) malonate. Journal of Synthetic Crystals, 2021,50(02):338–344.
 - **DOI**: 10.16553/j.cnki.issn1000-985x.2021.02.01.
- 34. Kresse, G.; Hafner, J. *Ab initio molecular dynamics for liquid metals.* Phys. Rev. B: Condens. Matter Mater. Phys. **1993**, 47(1): 558–561. **DOI:**10.1103/PhysRevB.47.558
- 35. Kresse, G.; Furthmüller, J. *Efficiency of ab-initio total energy calculations for metals and semiconductors using a plane-wave basis set.* Comput. Mater. Sci. **1996**, 6(1): 15–50.
 - DOI:10.1016/0927-0256(96)00008-0
- 36. Kresse, G.; Joubert, D. From ultrasoft pseudopotentials to the projector augmented-wave method. Phys. Rev. B: Condens. Matter Mater. Phys. 1999, 59, 1758–1775.
 - DOI:10.1103/PhysRevB.59.1758
- Blöchl, P. E. Projector augmented-wave method. Physical review. B, Condensed matter, 1994, 50(24).
 - DOI:10.1103/PhysRevB.50.17953
- J. P. Perdew, K. Burke, M. Ernzerhof. Generalized Gradient Approximation Made Simple. Physical review letters, 1996,77(18). DOI:10.1103/PhysRevLett.77.3865

- 39. Z Chen. Study of multilayer graphene and its adsorption to hydrogen atoms. Guangxi Normal University, Guilin, 2021.
- 40. SY Liu. Study on Stability, Kinetic Energy Density and Strong Interaction of Fullerene Isomers by Density Functional Theory. Hunan Normal University, Changsha, 2020.
- 41. H Jiang, WY Zhang. Density Functional Theory Method for Electronic Band Structure Calculation of Materials. China Science: Chemistry, **2020**,50(10):1344–1362.
 - DOI:10.1360/SSC-2020-0142
- S Maintz, VL Deringer, AL Tchougréeff, R Dronskowski. Analytic projection from plane-wave and PAW wavefunctions and application to chemical-bonding analysis in solids. J. Comput. Chem. 2013, 34, 2557–2567. DOI:10.1002/jcc.23424
- S Maintz, VL Deringer, AL Tchougréeff, R Dronskowski. LOBSTER: A tool to extract chemical bonding from planewave based DFT. J. Comput. Chem. 2016, 37, 1030–1035.
 DOI:10.1002/jcc.24300
- 44. G Wang, M Zhou, Goettel, J. T, Schrobilgen, G. J, J Su, J Li, Schlöder, T, Riedel, S. *Identification of an iridium-containing compound with a formal oxidation state of IX*. Nature: International weekly journal of science, 2014, 514(7523). DOI: 10.1038/nature13795.
- 45. XZ Shi, JL Wang, Z Cao. Electronic structure of monazite and adsorption mechanism of octylhydroxamic acid on its (100) surface. Chinese Journal of Nonferrous Metals. 2021,31(08):2238–2246. DOI: CNKI:SUN:ZYXZ.0.2021-08-023.
- R Dronskowski, PE Blöchl, Crystal orbital Hamilton populations (COHP): energy-resolved visualization of chemical bonding in solids based on density-functional calculations. J.Phys. Chem. 1993, 97, 8617–8624. DOI:10.1021/j100135a014
- 47. VL Deringer, AL Tchougréeff, R Dronskowski. *Crystal orbital Hamilton population (COHP) analysis as projected from plane-wave basis sets.* J. Phys. Chem. A **2011**, 115,5461–5466. **DOI:**10.1021/jp202489s
- 48. YL Liao, M Li, ZX Zhong. *Stability analysis of silicon nitride based on 'Materials Studio'*. Equipment manufacturing technology. **2018**(06):90–92.
 - DOI:10.1088/1475-7516/2018/06/026
- 49. BH Zhou, X Zuo. *Ab initio molecular dynamics of hydrogen diffusion in α-quartz.* Journal of Terahertz Science and Electronic Information, **2020**,18(02):325–329.
 - DOI: CNKI:SUN:XXYD.0.2020-02-028.
- 50. WL Luo, QQ Wang, W Ruan, AD Xie, LJ Shi, XL Wang, T Gao. Ab initio Molecular Dynamics of Pu-H₂ System. Chemical Research and Applications, 2019,31(04):593–597.
 DOI: CNKI:SUN:HXYJ.0.2019-04-001.
- 51. M Luo, SQ Liu, CY Ouyang. Ab initio molecular dynamics simulation of irradiation particles behavior in tungsten. The European Physical Journal B,2018,91(10). DOI:10.1140/epjb/e2018-90226-2.
- DS Sholl, JA Steckel. Density Functional Theory: A Practical Introduction. John Wiley & Sons, Inc:2009-03-30.
 DOI:10.1002/9780470447710
- T Zhou. Theoretical research on solvation growth and morphology control of TKX-50. North Central University, Tai-yuan, 2020.

Povzetek

V prispevku smo opisali napoved morfologije kristala cerijevega karbonata z uporabo simulacij na osnovi teorije gostotnega funkcionala (DFT). V fazi nukleacije se bo ketonska skupina v polivinilpirolidinu (PVP) preferenčno vezala na Ce3+ in tako tvorila kompleks, kar povzroči nastanek heterogenih nukleacijskih mest in s tem nukleacijo kristalov cerijevega karbonata. V fazi rasti je zaradi adsorpcije PVP največja verjetnost tvorbe (120) kristalnih ravnin v ravnotežju, kar povzroči nastanek heksagonalnih kristalov cerijevega karbonata. Eksperimentalno smo uspešno pripravili heksagonalne plasti kristalov cerijevega karbonata z uporabo PVP kot templata. Ugotovili smo, da metodo DFT lahko uporabimo za napoved morfologije kristalov cerijevega karbonata, s čemer pripomoremo k boljšemu razumevanju mehanizma rasti kristalov cerijevega karbonata in občutno zmanjšamo stroške eksperimenta.



Except when otherwise noted, articles in this journal are published under the terms and conditions of the Creative Commons Attribution 4.0 International License